RESEARCH ARTICLE | JULY 01 2025

Directly revealing double-resonance dynamics of second-harmonic generation in a quadratic microcavity

Jing Qiu ; Hao Li ; Yongzhi Tang; Zhuoran Hu ; Wenjun Ding; Shijie Liu; Juanjuan Lu; Wenjie Wan ; Yuanlin Zheng ; Xianfeng Chen

APL Photonics 10, 076102 (2025)
https://doi.org/10.1063/5.0276408

APL Photonics ARTICLE pubs.aip.org/aip/app

Directly revealing double-resonance dynamics of second-harmonic generation in a quadratic microcavity

Cite as: APL Photon. 10, 076102 (2025); doi: 10.1063/5.0276408
Submitted: 17 April 2025 • Accepted: 18 June 2025 •
Published Online: 1 July 2025

View Online Export Citation CrossMark

Jing Qiu,[1,2] Hao Li,[1] Yongzhi Tang,[1] Zhuoran Hu,[1] Wenjun Ding,[1] Shijie Liu,[1] Juanjuan Lu,[3] Wenjie Wan,[1,4] Yuanlin Zheng,[1,2,5,a)] and Xianfeng Chen[1,2,5,6,a)]

AFFILIATIONS

[1] State Key Laboratory of Photonics and Communications, School of Physics and Astronomy, Shanghai Jiao Tong University, Shanghai 200240, China
[2] Zhangjiang Laboratory, Shanghai 201210, China
[3] School of Information Science and Technology, ShanghaiTech University, Shanghai 201210, China
[4] University of Michigan-Shanghai Jiao Tong University Joint Institute, Shanghai Jiao Tong University, Shanghai 200240, China
[5] Shanghai Research Center for Quantum Sciences, Shanghai 201315, China
[6] Collaborative Innovation Center of Light Manipulations and Applications, Shandong Normal University, Jinan 250358, China

[a)] Authors to whom correspondence should be addressed: ylzheng@sjtu.edu.cn and xfchen@sjtu.edu.cn

ABSTRACT

High-quality (Q) microcavities, which significantly enhance wave mixings through optical resonances, play an important role in the investigation of light–matter interaction. For second-harmonic generation (SHG) in quadratic microcavities, satisfying a double-resonance condition is crucial for enhancing the nonlinear conversion. However, directly revealing a precise double-resonance condition can be demanding and has seldom been implemented. In this work, we introduce a method to synchronize the fundament wave and its second harmonic during the transmission measurement, and directly distinguish the double-resonance detuning. We also investigate the impact of each detuning on the cavity-enhanced SHG spectral line shape and intensity. The approach provides a method to help deeper understand of the nonlinear coupling processes and benefit research on cavity-enhanced nonlinear optics.

I. INTRODUCTION

In recent years, whispering-gallery-mode (WGM) microcavities,[1–4] based on total internal reflection, have gained significant attention as a versatile platform for optical physics and device applications, such as nonlinear optics,[5–10] lasing sources,[11,12] optical sensing,[13,14] quantum photonics,[15–18] and cavity optomechanics.[19,20] Due to their small mode volumes and ultralow optical losses, WGM microcavities enable efficient confinement of photons within the cavity for extended durations, thereby significantly enhancing the interaction between light and matter. They are particularly well-suited for investigation of a plethora of applications in nonlinear optics, including second-harmonic generation (SHG),[21–23] sum/difference frequency generation (SFG/DFG),[24,25] third-order harmonic generation (THG),[26,27] optical parametric oscillation (OPO),[28–30] and spontaneous parametric downconversion (SPDC).[31–33]

Efficient enhancement of nonlinear optical processes in a microcavity demands simultaneous fulfillment of several conditions: tight mode confinement, optimal mode overlap, long interaction length, large effective nonlinear coefficient, and phase matching condition. Moreover, resonances of the involved optical fields must occur simultaneously. Due to material and geometric dispersion, precise design and fabrication of resonators' structure are essential for ensuring simultaneous resonances at desired frequencies, which can be difficult. In fact, tuning mechanisms such as the thermo-optic[34] and electro-optic effects[35] are commonly employed to compensate resonance frequency shifts caused by fabrication imperfections. In SHG experiments, reaching optimized nonlinear conversion is widely regarded as an indicator of the condition where both the waves simultaneously satisfy the resonance requirements.[36–40] However, the condition can be vague with frequency detunings, and direct experimental measurement of the double-resonance detuning, which is important, has yet to be reported. The specific impact of double-resonance detuning on nonlinear effects has not been discussed.

In this Letter, we demonstrate an approach to visually observe the effect of double-resonance detuning on the cavity-enhanced SHG spectrum by synchronously scanning the FW and its SH to obtain the transmission spectrum of quadratic microcavities. The cavity-enhanced efficient SHG process is carried out in a periodically poled lithium niobate (PPLN) microring on the thin-film lithium niobate (TFLN) platform. Through SHG in another PPLN nonlinear waveguide, we can scan the WGM microcavity simultaneously in the FW and SH bands, achieving strict one-to-one correspondence between the FW and SH WGMs in the frequency domain and precisely determine the resonance detuning of each wave. We also leverage the thermal-optical effect to precisely manipulate the double-resonance detuning of the microcavity, directly revealing the double-resonance dynamics of SHG in the quadratic microcavity. This work paves a way for a deeper understanding of nonlinear processes in nonlinear microcavities, which may also be useful in non-Hermitian nonlinear photonics investigation.[41]

II. WGM MICROCAVITY DESIGN AND FABRICATION

We implement such a scheme to directly observe the double-resonance detuning of a WGM microcavity through a cavity-enhanced SHG scheme using a PPLN microring resonator on the z-cut TFLN platform, as shown in Fig. 1(a). The type I (oo-e) SHG process in the TFLN microring involves the fundamental transverse electric (TE_{00}) and magnetic (TM_{00}) modes at frequencies of ω_{FW} and ω_{SH} in the telecom and near-visible ranges, respectively. The perpendicularly polarized optical modes are particularly suited for proofing our scheme considering the large thermo-optical coefficient difference of LN.[34] In our design, the radius of the microring $R = 201.5\ \mu$m. The cross section of the microring is shown in Fig. 1(b). The thickness h of the TFLN is 520 nm, and the sidewall angle α of the ridge waveguide is 60°. The top width W and the etching depth t are 1.55 μm and 320 nm, respectively.

The significant spectral separation between the FW and SH modes presents a challenge for efficient dual-band coupling. To address this, we employ a single pulley waveguide to access efficient dual-band coupling to assist the transmission spectrum measurement in the both bands, which can be more effective than using an additional SH extraction waveguide.[42,43] We optimize the coupling parameters through the finite-difference time-domain (FDTD) simulation to satisfy the outstanding coupling in the near-infrared and the near-visible band and thereby access efficient dual-band coupling. In addition, we also performed a gap scan in the experiment to identify an appropriate coupling condition. The optimal width of the coupling waveguide W_w and the coupling gap is determined to be ~850 and 500 nm, respectively. The length of the pulley coupler is determined to be 67 μm ($\theta = 19°$), as shown in Fig. 1(c).

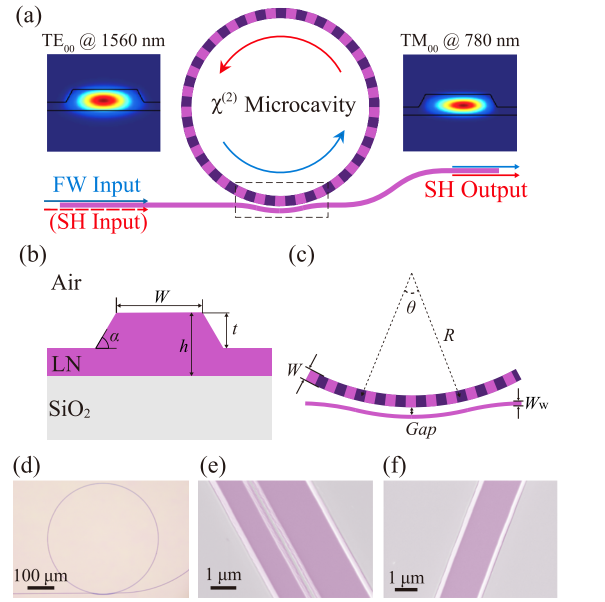

FIG. 1. (a) Schematic of the PPLN microring resonator on TFLN. Insets: simulated TE_{00} and TM_{00} mode profiles of FW and SH, respectively. (b) Schematic cross section of the nanowaveguide. (c) Diagram of the coupling region. (d) Optical image of the microring before electrical poling. Panels (e) and (f): false-color SEM images of the etched pulley coupler and waveguide (before poling), respectively.

The fabrication method for the TFLN microcavity is similar with that in Ref. 44. Electron beam lithography (EBL) using hydrogen-silsesquioxane (HSQ) photoresist is used to define the waveguide mask. Ridge waveguides are then fabricated using inductively coupled plasma (ICP) with argon ion milling. An optical image of the fabricated TFLN microring resonator is shown in Fig. 1(d), with zoomed-in scanning electron microscope (SEM) images of the coupling region and waveguide presented in Figs. 1(e) and 1(f). The smooth surface and sidewalls of the waveguide demonstrate the high quality of our fabrication process.

A first-order quasi-phase matching (QPM) condition for the type-I SHG process is achieved by periodically polling the TFLN microring along its radial direction. The QPM condition is $m_{SH} - 2m_{FW} - M = 0$ and $m = 2\pi nR/\lambda$, where m is the azimuthal number and n is the effective refractive index. Figure 2(a) plots the calculated poling period (Λ) with respect to the FW wavelength, showing that a poling period of 6.663 μm corresponds to the FW wavelength of 1560 nm with $M = 190$.

The poling process is initiated by depositing poling electrodes (10 nm thick titanium and 70 nm thick gold) with a tooth width of 2.2 μm onto the etched LN microring using EBL and lift-off technique; also see Fig. 2(b). The tooth width is designed to be smaller than half of the polling period to accommodate for domain broadening and to ensure a duty cycle of ~50%. The silicon substrate serves as the electrical ground. Periodic ferroelectric domain inversion is then achieved by applying a strong electric field to the crystal through the electrodes, i.e., electric poling, at an elevated temperature of 260 °C. A period of ~6.67 μm with a duty cycle of ~50% is achieved, as shown in Fig. 2(c).

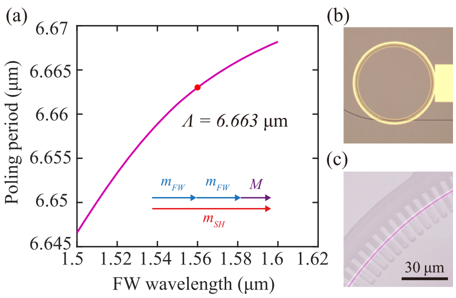

FIG. 2. (a) Numerical simulation of the poling period for first-order type I QPM, with $\Lambda = 6.663$ μm@1560 nm. The inset illustrates QPM conditions. (b) Microscope image of the radial poling electrodes. (c) False-color SEM image of a part of the PPLN microring resonator after HF etching.

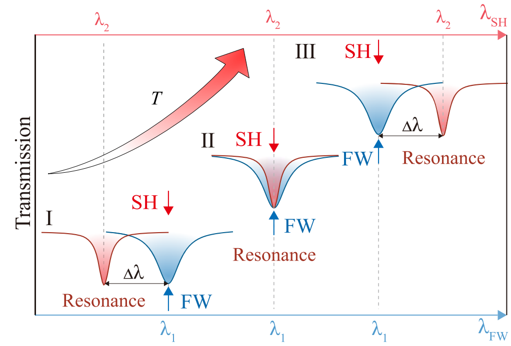

FIG. 3. Schematic of the dynamic resonance chasing. λ_1 and λ_2 are the central wavelengths of the cavity resonances. The blue and red arrows indicate the inject FW and generated SH wavelengths, respectively.

III. THEORY

To gain more physical insight, we provide a detail discussion on SHG theoretical modeling. For SHG in a resonant nonlinear cavity, the wave amplitude of the injected FW, A_{FW}, and the generated SH, A_{SH}, can be modeled according to the coupled mode theory,[5]

$$\frac{\mathrm{d}A_{FW}}{\mathrm{d}t} = \left(i\Delta\omega_1 - \frac{\kappa_{1\mathrm{i}} + \kappa_{1e}}{2}\right)A_{FW} + \sqrt{\kappa_{1e}}A_{FW}^{in} - ig^{*}A_{FW}{}^{*}A_{SH}, \quad (1)$$

$$\frac{\mathrm{d}A_{SH}}{\mathrm{d}t} = \left(i\Delta\omega_2 - \frac{\kappa_{2\mathrm{i}} + \kappa_{2e}}{2}\right)A_{SH} + igA_{FW}{}^{2}. \quad (2)$$

These cavity resonances are modeled by the photon decay rate, κ ($\kappa = 1/\tau$, τ is the photon lifetime), including the internal rate, κ_i, and the external rate, κ_e, with a frequency detuning of $\Delta\omega_i$ from its central resonance of ω_i ($i = 1, 2$ represents the FW and SH, respectively). The detuning is $\Delta\omega_1 = \omega_{FW} - \omega_1$, $\Delta\omega_2 = \omega_{SH} - \omega_2$. In addition, g is the coupling coefficient, which is proportional to the mode area, mode overlap, and effective nonlinear coefficient. Under the small-signal approximation and considering the steady state ($\mathrm{d}A/\mathrm{d}t = 0$), the generated SH power is

$$P_{\mathrm{SH}} = \frac{|g|^2}{\omega_2\omega_1^2}\frac{4Q_2^2/Q_{2e}}{4Q_2^2(\Delta\omega_2/\omega_2)^2 + 1}\frac{16Q_1^4/Q_{1e}{}^2}{\left[4Q_1^2(\Delta\omega_1/\omega_1)^2 + 1\right]^2}P_{\mathrm{FW}}{}^2, \quad (3)$$

where Q_i and Q_{ie} stand for the loaded quality factor and external (coupling related) quality factor, respectively. P_{SH} is affected by resonances of both the FW and SH, i.e., the double-resonance condition. When $\Delta\omega_2 = \Delta\omega_1 = 0$, the FW and SH waves simultaneously match the resonant modes, fulfilling the double-resonance condition, and yield the maximum output.

In general, the FW and SH resonances are offset. The offset can be manipulated via simple temperature control, thanks to the difference thermal-optic response of both the resonances. The dynamic resonance chasing process is illustrated in Fig. 3. When the input FW is resonant with a cavity FW mode (λ_1), the SH signal is generally not precisely resonant with the corresponding SH mode (λ_2) of the cavity due to dispersion (state I). Considering the TFLN microring cavity, the extraordinary refractive index of LN has a larger thermal-optical coefficient than the ordinary one. Taking the thermal-optical effect, both the FW and SH resonances undergo redshifts as the temperature increases, and the wavelength of SH resonance should increase to catch the resonant mode because the SH (e) mode moves faster than the FW (o) mode (states I–III). The SH signal can align with the SH mode at a specific FW frequency. The double-resonance condition is then fulfilled, where the SH mode frequency is twice the frequency of the FW mode and both the input FW and generated SH waves are correspondingly resonant (state II). As the temperature increases, the SH resonance (λ_2) surpasses the SH signal (λ_{SH}) while the FW is kept resonant ($\lambda_{FW} = \lambda_1$). At this point, the double-resonance condition is no longer satisfied (state III). $\Delta\lambda = \lambda_1 - 2\lambda_2$ denotes double-resonance detuning. The evolution of nonlinear SHG is observed by modulating double-resonance detuning. This is fundamentally important in the coupling mode equation. However, precisely determining the resonance detuning in an experiment can be demanding and has seldom been reported.

IV. EXPERIMENT AND RESULTS

To solve this problem, we propose to visually observe the double-resonance detuning by synchronously scanning the transmission spectrum at the FW and SH bands, that is, synchronous dual-band scanning. The experimental setup is shown in Fig. 4(a). An external cavity tunable laser at the telecom bands (Toptica CTL) serves as the source. The input laser is first amplified by an erbium-doped optical fiber amplifier (EDFA) and then divided into two beams by a 90%:10% beam splitter (BS). One beam, path I, adjusted by a polarization controller (PC) is coupled into a PPLN ridge waveguide using lensed fiber. The SH signal is used to scan transmission spectra of the WGM microring at the SH band. To obtain a wideband tunable SH source, an array of PPLNWG with different topwidths for various QPM wavelengths is used. Efficient SHG can be performed in a wide range using different PPLNWGs. In our experiment, the dual-band (FW and SH) scanning can be performed at all resonances in a wide bandwidth from 1530 to 1580 nm. The series of the generated SH spectrum through our PPLNWG array is shown in Fig. 4(b). It should be noted that broadband SHG can also be achieved using a chirped PPLN waveguide; however, the PPLNWG array offers much higher frequency conversion efficiency in the experiment, which is more favorable for

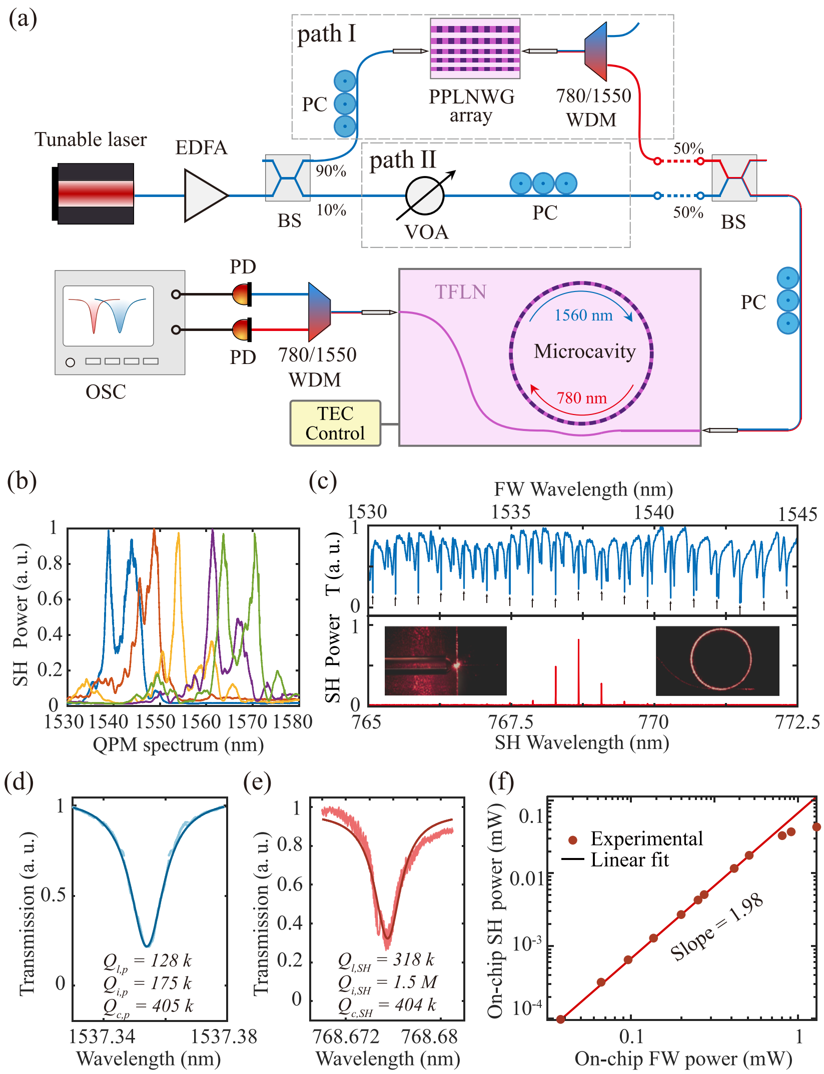

FIG. 4. (a) Experimental setup for FW-SH dual-band transmission measurement of the TFLN microring. EDFA (erbium-doped fiber amplifier); BS (beam splitter); PC (polarization controller); PPLNWG array: PPLN ridge waveguide array, VOA (variable optical attenuator); WDM (wavelength-division multiplexer); TEC (thermoelectric cooler); PD (photodetector); and OSC (oscilloscope). (b) A series of typical SH spectra in a PPLNWG array with different colors corresponding to different waveguide top widths. (c) SH signals (red) vs the FW input (blue). Insets: images of generated SH scattering from the top and the edge. (d) and (e) Resonance spectra of FW (TE_{00}) and SH (TM_{00}) WGM modes. (f) On-chip SHG power and on-chip FW power relation.

synchronous dual-band scanning. The other beam, path II, incorporated a variable optical attenuator (VOA) and a PC is used to sweep the transmission spectra of the microring at the FW wavelengths. Light from both paths is then combined by a 50%:50% BS and via a lensed fiber launched into the TFLN microring, which is held on a feedback-controlled heater with a tuning range from −10 to 75 °C at a resolution of 0.01 °C. The temperature controller ensures precise control of the device temperature to manipulate the double-resonance detuning. The fiber-to-chip coupling loss at FW and SH is estimated to be 8.5 and 13.0 dB/facet, respectively. The output is coupled out via another lensed fiber and then filtered by a wavelength-division multiplexer (WDM) and detected using photodetectors (PDs).

Figure 4(c) shows the SH signal spectrum by sweeping the TE-polarized FW with an input power of 1 mW. The thermal broadening of the WGM resonance is negligible. The arrows in the transmission spectrum indicate the TE_{00} mode family, with a free spectral range (FSR) of 0.80 nm, consistent with the theoretical prediction. The input FW and generated SH signal modes satisfying perfect double-resonance and QPM conditions are observed at the wavelengths of 1537.354 and 768.677 nm, respectively. The deviation from the theoretical value is attributed to the non-uniformity in film thickness. The insets show the image of the scattered SHG from the TFLN microring and the waveguide output. Figures 4(d) and 4(e) show resonance spectra of the FW and SH WGMs, respectively. The FW (SH) resonance is slightly under-coupled (over-coupled) with a loaded Q factor (Q_L) of 1.28×10^5 (3.18×10^5). The Q factor is several times lower than state-of-the-art PPLN microrings with a similar geometry.[31] Although a smaller Q factor is detrimental to SHG conversion, it gives rise to greater system stability for observing the double-resonance dynamics, as the thermal effect is more stable.

In the experiment, the on-chip SHG efficiency is optimized by finely tuning the resonance frequencies of the FW and SH modes via temperature control. The relationship between the optimized on-chip SH and FW power is shown in Fig. 4(f). In the undepleted pump regime ($P_{FW} < 550\ \mu$W), a linear-fitted slope of 1.98 confirmed the expected quadratic scaling and a small-signal normalized SHG efficiency of 7085%/W. According to Ref. 36, when the critical coupling and double-resonance conditions for FW and SH modes are fulfilled, maximum SHG conversion efficiency can be achieved. The theoretically attainable maximum SHG efficiency in our PPLN microring device is ∼25 300%/W, based on the calculation in Ref. 36. The discrepancy is possibly attributed to the imperfect QPM grating, non-ideal coupling between the microring and the bus waveguide.

We directly distinguish the double-resonance detuning by synchronously scanning the FW and SH WGM mode transmission spectra. The energy conservation during SHG guarantees that the frequency of the SH light generated in the PPLNWG in path I and the FW light in path II have a strict one-to-one correspondence. This ensures an accurate measurement of the double-resonance detuning in the nonlinear microcavity, compared to the method using separate visible and near-infrared tunable lasers for the transmission measurement. The distinct thermal shifts of the two interacting modes then allow us to leverage temperature tuning to modulate double-resonance detuning. Under the same temperature conditions, we disconnect path I and obtain the cavity generated SH signal spectrum and the FW transmission spectrum of the microring. The FW transmission spectrum is used to relate the SH signal spectrum to the double-resonance spectrum obtained by synchronously scanning path I and path II. The accuracy of our method is, therefore, ultrahigh, which is also adoptable for ultrahigh-Q nonlinear microcavities in the same manner.

The experimental measurement of the dynamic resonance chasing and the corresponding SHG yielding in the TFLN microring is shown in Fig. 5. We select different double-resonance detuning conditions and plot the corresponding FW-SH dual-band transmission and the generated SH signal spectra. When the double-resonance detuning is large (i.e., in the fully single-resonance regime), the SH signal spectrum exhibits a double-peak structure, with the two peaks corresponding to the resonance of each FW and SH mode, as shown in Fig. 5(a). The FW single-resonance yields a stronger intensity than the SH single-resonance because, at the SH single-resonance wavelength, nearly no FW light is coupled into the microring. As the temperature increases, the SH resonance mode gradually approaches and catches the FW resonance mode with reducing the double-resonance detuning, as depicted in Figs. 5(b)–5(e). Consequently, the peak values of the two peaks gradually converge and the SH signal spectrum evolves into a single-peak mode. The peak of the SH signal is closer to the SH resonance wavelength due to the fact that the SH mode has a higher loaded Q factor in the experiment. Comparing the SH intensities in Figs. 5(a) and 5(e), the enhancement factor under the double-resonance condition is two orders of magnitude higher than that under the single-resonance condition. It should be noted that the fitting of the generated SH spectra is based on the prediction of Eq. (3), where both the resonance detuning is preknown according to our FW-SH dual-band scanning during the transmission measurement. In addition, this approach holds promise for application to other nonlinear optical processes, such as SFG, DFG, and OPO. Due to a lower conversion efficiency, electromagnetically induced transparency such as transmission spectrum[45] or mode splitting[46] induced by strong

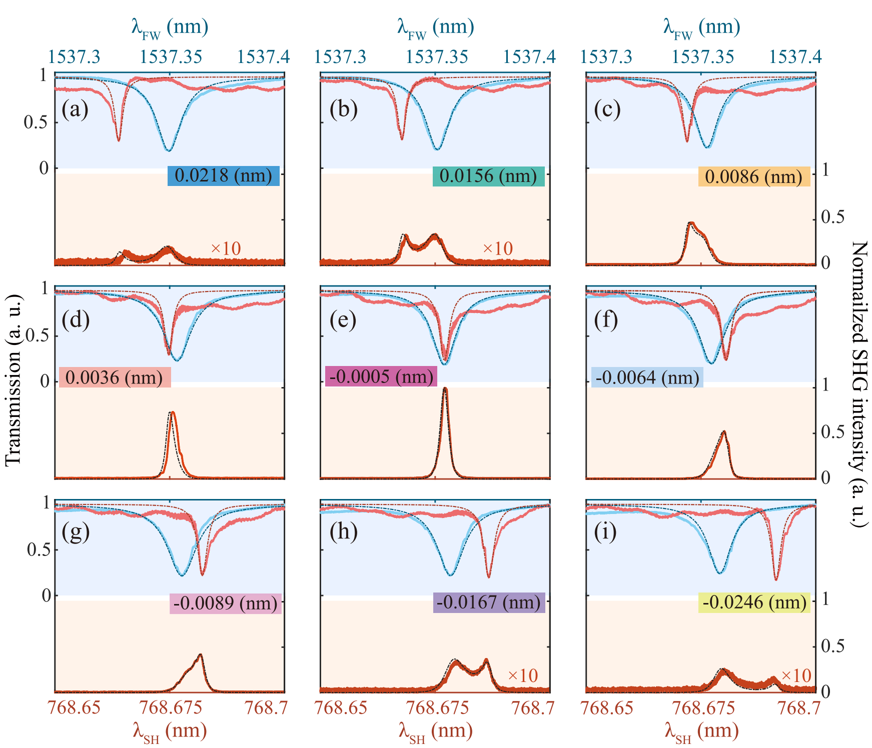

FIG. 5. (a)–(i) Transmission spectra at FW-SH dual bands and generated SH signal spectra with different double-resonance detuning. The upper curve shows the transmission spectra of the FW (blue) and SH (red) WGMs under synchronous scanning, with the dashed lines indicating Lorentzian fitting. The lower curve is the generated SH signal spectra, with the dashed lines corresponding to the calculations based on Eq. (3). (Intensity is not to scale.).

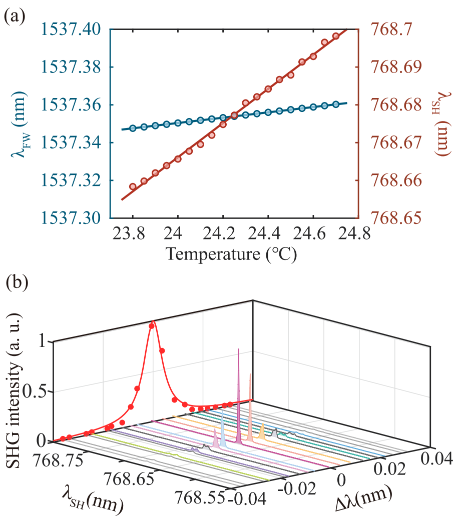

FIG. 6. (a) Resonance shifts vs the temperature for FW and SH WGMs. (b) SH signal spectra with different resonance detuning ($\Delta\lambda$).

coupling between optical modes of different colors was not observed in our experiment.

The temperature dependence of the FW and SH resonance frequencies, obtained by fitting the FW and SH transmission spectra, is shown in Fig. 6(a). Both resonances redshift with the increased temperature due to the thermo-optic effect and thermal expansion.[47] At a temperature of 24.24 °C, the double-resonance condition is satisfied and the FW resonance wavelength is 1537.354 nm. Figure 6(b) displays a set of SH signal spectra at different double-resonance detuning ($\Delta\lambda$). We plot the peak SHG intensity for different double-resonance detuning, with a Lorentzian linewidth of 0.009 nm. As expected, the peak SHG intensity occurs under the double-resonance condition,[36–39] where both FW and SH waves are enhanced in the microcavity.

Before our study, the dynamics of double-resonance was only inferred from the SH spectrum but has not been directly observed in experiment. By synchronously scanning the resonance of the FW and SH WGMs, we can visually observe the influence of double-resonance on the SHG efficiency and spectral line shape. The result also shows without ambiguity that the precise double-resonance condition is a must for efficient cavity-enhanced SHG. Our method reveals the exact resonance detuning during the nonlinear wave mixing, which would help gain insight into the non-Hermitian degeneracies in nonlinear photonics.

V. CONCLUSION

In summary, we have proposed and demonstrated a method to directly distinguish double-resonance detuning of the SHG process in a nonlinear microcavity by synchronized scanning of the cavity in the FW and SH dual bands. It offers the key advantage that the scanning frequency of FW and SH waves is rigorous with one-to-one correspondence, which is critical for testing exact double-resonance detuning. We also leverage the thermal-optical effect to precisely manipulate the double-resonance detuning of the microcavity, directly revealing the double-resonance dynamics of SHG in the quadratic microcavity. This work would be beneficial to applications such as cavity-enhanced frequency conversion and non-Hermitian nonlinear optics.

ACKNOWLEDGMENTS

This work was supported by the National Key Research and Development Program of China (Grant Nos. 2022YFA1205100 and 2023YFA1407200), the National Natural Science Foundation of China (Grant No. 12192252), the Science and Technology Commission of Shanghai Municipality (Grant No. 24JD1401700), the Shanghai Municipal Science and Technology Major Project (Grant No. 2019SHZDZX01-ZX06), the Guangdong Provincial Quantum Science Strategic Initiative (Grant No. GDZX2403003), and the Yangyang Development Fund.

AUTHOR DECLARATIONS

Conflict of Interest

The authors have no conflicts to disclose.

Author Contributions

Jing Qiu: Data curation (lead); Formal analysis (lead); Investigation (lead); Methodology (equal); Writing – original draft (lead). **Hao Li**: Investigation (supporting); Methodology (equal). **Yongzhi Tang**: Formal analysis (supporting); Investigation (supporting). **Zhuoran Hu**: Investigation (supporting); Validation (supporting). **Wenjun Ding**: Investigation (supporting). **Shijie Liu**: Investigation (supporting); Validation (supporting). **Juanjuan Lu**: Methodology (supporting). **Wenjie Wan**: Methodology (supporting). **Yuanlin Zheng**: Conceptualization (lead); Funding acquisition (equal); Project administration (equal); Resources (equal); Supervision (equal); Writing – review & editing (lead). **Xianfeng Chen**: Conceptualization (supporting); Funding acquisition (equal); Project administration (equal); Resources (equal); Supervision (equal).

DATA AVAILABILITY

The data that support the findings of this study are available within the article.

REFERENCES

[1]K. J. Vahala, "Optical microcavities," Nature **424**, 839–846 (2003).

[2]R.-R. Xie, G.-Q. Li, F. Chen, and G.-L. Long, "Microresonators in lithium niobate thin films," Adv. Opt. Mater. **9**, 2100539 (2021).

[3]G. Lin, A. Coillet, and Y. K. Chembo, "Nonlinear photonics with high-Q whispering-gallery-mode resonators," Adv. Opt. Photonics **9**, 828–890 (2017).

[4]P. Liu, H. Wen, L. Ren, L. Shi, and X. Zhang, "$\chi^{(2)}$ nonlinear photonics in integrated microresonators," Front. Optoelectron. **16**, 18 (2023).

[5]X. Zhang, Q.-T. Cao, Z. Wang, Y.-x. Liu, C.-W. Qiu, L. Yang, Q. Gong, and Y.-F. Xiao, "Symmetry-breaking-induced nonlinear optics at a microcavity surface," Nat. Photonics **13**, 21–24 (2018).

[6]T. P. McKenna, H. S. Stokowski, V. Ansari, J. Mishra, M. Jankowski, C. J. Sarabalis, J. F. Herrmann, C. Langrock, M. M. Fejer, and A. H. Safavi-Naeini,

"Ultra-low-power second-order nonlinear optics on a chip," Nat. Commun. **13**, 4532 (2022).
[7]J.-Q. Wang, Y.-H. Yang, M. Li, X.-X. Hu, J. B. Surya, X.-B. Xu, C.-H. Dong, G.-C. Guo, H. X. Tang, and C.-L. Zou, "Efficient frequency conversion in a degenerate $\chi^{(2)}$ microresonator," Phys. Rev. Lett. **126**, 133601 (2021).
[8]G. Zhao, J. Zhu, J. Hou, Y. Chen, J. Lin, Y. Cheng, X. Chen, Y. Zheng, and W. Wan, "Controllable eit-like mode splitting in a chiral microcavity," Opt. Lett. **48**, 755–758 (2023).
[9]H. Hwang, K. Ko, M. R. Nurrahman, K. Moon, J. J. Ju, S.-W. Han, H. Jung, M.-K. Seo, and H. Lee, "A wide-spectrum mid-infrared electro-optic intensity modulator employing a two-point coupled lithium niobate racetrack resonator," APL Photonics **10**, 016116 (2025).
[10]K. Pathak and R. Pant, "Brillouin laser pumped tunable low-threshold mid-IR Kerr comb at 2 μm," APL Photonics **9**, 100803 (2024).
[11]G.-Q. Wei, X.-D. Wang, and L.-S. Liao, "Recent advances in organic whispering-gallery mode lasers," Laser Photonics Rev. **14**, 2000257 (2020).
[12]X. Liu, X. Yan, Y. Liu, H. Li, Y. Chen, and X. Chen, "Tunable single-mode laser on thin film lithium niobate," Opt. Lett. **46**, 5505–5508 (2021).
[13]N. Toropov, G. Cabello, M. P. Serrano, R. R. Gutha, M. Rafti, and F. Vollmer, "Review of biosensing with whispering-gallery mode lasers," Light: Sci. Appl. **10**, 42 (2021).
[14]X. Wang, T. Yuan, J. Wu, Y. Chen, and X. Chen, "Enhanced temperature sensing by multi-mode coupling in an on-chip microcavity system," Laser Photonics Rev. **18**, 2300760 (2024).
[15]L. Wang, C. Wang, J. Wang, F. Bo, M. Zhang, Q. Gong, M. Lončar, and Y.-F. Xiao, "High-Q chaotic lithium niobate microdisk cavity," Opt. Lett. **43**, 2917–2920 (2018).
[16]Z. Ma, J.-Y. Chen, Z. Li, C. Tang, Y. M. Sua, H. Fan, and Y.-P. Huang, "Ultrabright quantum photon sources on chip," Phys. Rev. Lett. **125**, 263602 (2020).
[17]M. Li, Y.-L. Zhang, H. X. Tang, C.-H. Dong, G.-C. Guo, and C.-L. Zou, "Photon-photon quantum phase gate in a photonic molecule with $\chi^{(2)}$ nonlinearity," Phys. Rev. Appl. **13**, 044013 (2020).
[18]J.-Y. Chen, Z. Li, Z. Ma, C. Tang, H. Fan, Y. M. Sua, and Y.-P. Huang, "Photon conversion and interaction in a quasi-phase-matched microresonator," Phys. Rev. Appl. **16**, 064004 (2021).
[19]M. Aspelmeyer, T. J. Kippenberg, and F. Marquardt, "Cavity optomechanics," Rev. Mod. Phys. **86**, 1391–1452 (2014).
[20]Z. Fang, S. Haque, J. Lin, R. Wu, J. Zhang, M. Wang, J. Zhou, M. Rafa, T. Lu, and Y. Cheng, "Real-time electrical tuning of an optical spring on a monolithically integrated ultrahigh Q lithium nibote microresonator," Opt. Lett. **44**, 1214–1217 (2019).
[21]J. U. Fürst, D. V. Strekalov, D. Elser, M. Lassen, U. L. Andersen, C. Marquardt, and G. Leuchs, "Naturally phase-matched second-harmonic generation in a whispering-gallery-mode resonator," Phys. Rev. Lett. **104**, 153901 (2010).
[22]X. Lu, G. Moille, Q. Li, D. A. Westly, A. Singh, A. Rao, S.-P. Yu, T. C. Briles, S. B. Papp, and K. Srinivasan, "Efficient telecom-to-visible spectral translation through ultralow power nonlinear nanophotonics," Nat. Photonics **13**, 593–601 (2019).
[23]J. Chen, C. Tang, M. Jin, Z. Li, Z. Ma, H. Fan, S. Kumar, Y. M. Sua, and Y. Huang, "Efficient frequency doubling with active stabilization on chip," Laser Photonics Rev. **15**, 2100091 (2021).
[24]X. Ye, S. Liu, Y. Chen, Y. Zheng, and X. Chen, "Sum-frequency generation in lithium-niobate-on-insulator microdisk via modal phase matching," Opt. Lett. **45**, 523–526 (2020).
[25]J. Zhu, X. Sun, T. Ding, Y. Tang, S. Liu, Y. Zheng, and X. Chen, "Sum-frequency generation in a high-quality thin film lithium niobate microdisk via cyclic quasi-phase matching," J. Opt. Soc. Am. B **40**, 44–49 (2023).
[26]J. Lin, N. Yao, Z. Hao, J. Zhang, W. Mao, M. Wang, W. Chu, R. Wu, Z. Fang, L. Qiao, W. Fang, F. Bo, and Y. Cheng, "Broadband quasi-phase-matched harmonic generation in an on-chip monocrystalline lithium niobate microdisk resonator," Phys. Rev. Lett. **122**, 173903 (2019).
[27]K. Sasagawa and M. Tsuchiya, "Highly efficient third harmonic generation in a periodically poled MgO:$LiNbO_3$ disk resonator," Appl. Phys. Express **2**, 122401 (2009).
[28]T. Beckmann, H. Linnenbank, H. Steigerwald, B. Sturman, D. Haertle, K. Buse, and I. Breunig, "Highly tunable low-threshold optical parametric oscillation in radially poled whispering gallery resonators," Phys. Rev. Lett. **106**, 143903 (2011).
[29]J. U. Fürst, D. V. Strekalov, D. Elser, A. Aiello, U. L. Andersen, C. Marquardt, and G. Leuchs, "Low-threshold optical parametric oscillations in a whispering gallery mode resonator," Phys. Rev. Lett. **105**, 263904 (2010).
[30]J. Lu, A. Al Sayem, Z. Gong, J. B. Surya, C.-L. Zou, and H. X. Tang, "Ultralow-threshold thin-film lithium niobate optical parametric oscillator," Optica **8**, 539–544 (2021).
[31]U. A. Javid, J. Ling, J. Staffa, M. Li, Y. He, and Q. Lin, "Ultrabroadband entangled photons on a nanophotonic chip," Phys. Rev. Lett. **127**, 183601 (2021).
[32]B.-Y. Xu, L.-K. Chen, J.-T. Lin, L.-T. Feng, R. Niu, Z.-Y. Zhou, R.-H. Gao, C.-H. Dong, G.-C. Guo, Q.-H. Gong, Y. Cheng, Y.-F. Xiao, and X.-F. Ren, "Spectrally multiplexed and bright entangled photon pairs in a lithium niobate microresonator," Sci. China: Phys., Mech. Astron. **65**, 294262 (2022).
[33]Z. Ma, J.-Y. Chen, M. Garikapati, Z. Li, C. Tang, Y. M. Sua, and Y.-P. Huang, "Highly efficient and pure few-photon source on chip," Phys. Rev. Appl. **20**, 044033 (2023).
[34]L. Moretti, M. Iodice, F. G. Della Corte, and I. Rendina, "Temperature dependence of the thermo-optic coefficient of lithium niobate, from 300 to 515 K in the visible and infrared regions," J. Appl. Phys. **98**, 036101 (2005).
[35]A. Guarino, G. Poberaj, D. Rezzonico, R. Degl'Innocenti, and P. Günter, "Electro–optically tunable microring resonators in lithium niobate," Nat. Photonics **1**, 407–410 (2007).
[36]J. Lu, J. B. Surya, X. Liu, A. W. Bruch, Z. Gong, Y. Xu, and H. X. Tang, "Periodically poled thin-film lithium niobate microring resonators with a second-harmonic generation efficiency of 250,000%/W," Optica **6**, 1455–1460 (2019).
[37]J. Lu, M. Li, C.-L. Zou, A. Al Sayem, and H. X. Tang, "Toward 1% single-photon anharmonicity with periodically poled lithium niobate microring resonators," Optica **7**, 1654–1659 (2020).
[38]X. Wu, Z. Hao, L. Zhang, D. Jia, R. Ma, C. Tao, F. Gao, F. Bo, G. Zhang, and J. Xu, "Second-harmonic generation with a 440,000%W^{-1} conversion efficiency in a lithium niobate microcavity without periodic poling," Laser Photonics Rev. **18**, 2300951 (2024).
[39]H. Du, X. Zhang, H. Lv, J. Lin, L. Wang, and F. Chen, "High-efficiency second harmonic generation in a micro-resonator on dual-layered lithium niobate," Opt. Lett. **49**, 391–394 (2024).
[40]J.-Y. Chen, Z.-H. Ma, Y. M. Sua, Z. Li, C. Tang, and Y.-P. Huang, "Ultra-efficient frequency conversion in quasi-phase-matched lithium niobate microrings," Optica **6**, 1244–1245 (2019).
[41]J. Hou, J. Zhu, R. Ma, B. Xue, Y. Zhu, J. Lin, X. Jiang, Y. Zheng, X. Chen, Y. Cheng, L. Ge, and W. Wan, "Enhanced frequency conversion in parity-time symmetry line," Phys. Rev. Lett. **132**, 256902 (2024).
[42]A. W. Bruch, X. Liu, X. Guo, J. B. Surya, Z. Gong, L. Zhang, J. Wang, J. Yan, and H. X. Tang, "17,000%/W second-harmonic conversion efficiency in single-crystalline aluminum nitride microresonators," Appl. Phys. Lett. **113**, 131102 (2018).
[43]X. Guo, C.-L. Zou, and H. X. Tang, "Second-harmonic generation in aluminum nitride microrings with 2500%/W conversion efficiency," Optica **3**, 1126–1131 (2016).
[44]M. Zhang, C. Wang, R. Cheng, A. Shams-Ansari, and M. Lončar, "Monolithic ultra-high-Q lithium niobate microring resonator," Optica **4**, 1536–1537 (2017).
[45]Y. Zheng, J. Yang, Z. Shen, J. Cao, X. Chen, X. Liang, and W. Wan, "Optically induced transparency in a micro-cavity," Light: Sci. Appl. **5**, e16072 (2016).
[46]X. Guo, C.-L. Zou, H. Jung, and H. X. Tang, "On-chip strong coupling and efficient frequency conversion between telecom and visible optical modes," Phys. Rev. Lett. **117**, 123902 (2016).
[47]T. Carmon, L. Yang, and K. J. Vahala, "Dynamical thermal behavior and thermal self-stability of microcavities," Opt. Express **12**, 4742–4750 (2004).